Met. Mater. Int., Vol. 23, No. 3 (2017), pp. 610~617
doi: 10.1007/s12540-017-6510-6

Si-FeSi$_2$/C Nanocomposite Anode Materials Produced by Two-Stage High-Energy Mechanical Milling

Yun Mo Yang [1], Chadrasekhar Loka[1,2], Dong Phil Kim[1], Sin Yong Joo[1], Sung Whan Moon[3], Yi Sik Choi[3], Jung Han Park[4], and Kee-Sun Lee[1,*]

[1]Department of Advanced Materials Engineering, Kongju National University, Gongju 32588, Republic of Korea
[2]Smart Natural Space Research Center, Kongju National University, Gongju 32588, Republic of Korea
[3]Research Institute, Sapphire Technology Co., Hwaseong 18623, Republic of Korea
[4]Rare Isotope Accelerator Promotion Team, Ministry of Science, ICT and Future Planning,
Gwacheon 13809, Republic of Korea

(received date: 19 July 2016 / accepted date: 17 October 2016)

High capacity retention Silicon-based nanocomposite anode materials have been extensively explored for use in lithium-ion rechargeable batteries. Here we report the preparation of Si-FeSi$_2$/C nanocomposite through scalable a two-stage high-energy mechanical milling process, in which nano-scale Si-FeSi$_2$ powders are besieged by the carbon (graphite/amorphous phase) layer; and investigation of their structure, morphology and electrochemical performance. Raman analysis revealed that the carbon layer structure comprised of graphitic and amorphous phase rather than a single amorphous phase. Anodes fabricated with the Si-FeSi$_2$/C showed excellent electrochemical behavior such as a first discharge capacity of 1082 mAh g^{-1} and a high capacity retention until the 30th cycle. A remarkable coulombic efficiency of 99.5% was achieved within a few cycles. Differential capacity plots of the Si-FeSi$_2$/C anodes revealed a stable lithium reaction with Si for lithiation/delithiation. The enhanced electrochemical properties of the Si-FeSi$_2$/C nanocomposite are mainly attributed to the nano-size Si and stable solid electrolyte interface formation and highly conductive path driven by the carbon layer.

Keywords: anode materials, lithium-ion battery, silicon, high-energy mechanical milling, raman spectra

1. INTRODUCTION

Nowadays, rechargeable lithium-ion batteries (LIBs) are extensively used as a convenient power source for various applications such as portable electronics, hybrid electric vehicles (HEVs), plug-in hybrid electric vehicles (PHEVs), and electric vehicles (EVs) [1-5]; because LIBs have high energy and power densities, high operating voltages and a low self-discharge rate [6-8]. Nevertheless, the increasing need of LIBs in power storage installations is not satisfied by the existing commercial graphite-based anode materials because of their low theoretical specific capacity, which is about 370 mAh g^{-1} [7,9]. In order to fulfill the demands of emerging types of electronic devices, alloy-type anode materials with high theoretical capacity and low operating voltage such as silicon (Si) and tin (Sn), antimony (Sb), and aluminum (Al) have been extensively explored to further increase the energy densities of LIBs. In the past decade, Si has been regarded as one of the most promising alloy-type high capacity anode materials with a theoretical capacity of 4200 mAh g^{-1}, because each Si atom accommodates up to 4.4 lithium atoms to form the $Li_{22}Si_5$ alloy [10-13]. Albeit the Si is the promising choice of anode materials, electrode pulverization and serious capacity fade during lithiation and delithiation owing to large volume changes (~400% volume expansion and contraction) and the stress generated during this process are shortening its cycle life (capacity retention) and finally leading to cell failure. Numerous efforts have been devoted to alleviate the detrimental effects of the large volume changes with various nano-structures of the Si such as nanowires [14], nanotubes [15], hollow nanospheres [16], nano films [17], and nanocomposites [18-20]. In addition, multiphase composite materials such as metallic nanohybrids and carbonaceous nanohybrids have been exploited for their ability to accommodate the volume change and enhance the electrical conductivity [21-23]. These approaches are associated with critical methods to reduce Si size, improve electrical conductivity and form a stable solid electrolyte interface (SEI).

In the present study, we prepare a Si-FeSi$_2$/Carbon nanocomposite in which the nano-scale Si crystals are finely dispersed in less-active matrix phase (FeSi$_2$) in the form of Si-FeSi$_2$ and then the Si-FeSi$_2$ is structured with carbon by using

---

*Corresponding author: kslee@kongju.ac.kr

high-energy mechanical milling (HEMM). In this approach, capacity retention is expected to be enhanced due to formation of the highly elastic silicide phase $FeSi_2$, which could effectively buffer the volume change of the nano-sized active Si during lithiation/delithiation (cycling). In addition, the added carbon can contribute to enhance the electrical conductivity and form stable SEI; because the carbon layer can improve an electrical connectivity between the active materials and will introduce stable SEI on the carbon layer surface instead of the Si. HEMM can be an effective process for synthesizing nanostructured composite materials [24-27]. Moreover, it is effective for the large-scale synthesis because of its low cost and operational simplicity. However, contamination is a serious problem that usually occurs during HEMM [28]. The contamination resulting from the interaction between the milling medium and vial leads to poor cycle performance. Using a 'seasoned' milling vial in which the medium is coated with the processing powders can be a promising method to minimize the contamination. Moreover, shortening the milling time and using the pre-alloyed powders for milling might be beneficial. Consequently, this study covers the preparation of nanocomposite Si-$FeSi_2$/C anode materials by using a two-stage HEMM and the evaluation of their electrochemical properties.

2. EXPERIMENTAL PROCEDURE

2.1. Synthesis of nanocomposite anode material

Si and Fe powders were taken as starting raw materials with an atomic percentage of 84% and 16%, respectively. The Si-$FeSi_2$ master alloy (ingot) was prepared by the induction melting process. The master alloy was then mechanically crushed using jaw crusher and sieved using a 106 μm sized mesh. Subsequently, the pre-alloyed powder was mechanically milled using a Simoloyer CM01 (Zoz GmbH, Germany) high-energy mechanical milling (HEMM) system controlled by MALTOZ-software. Prior to the milling, the processing vial was sealed under argon atmosphere. A ball-to-powder weight ratio of 15:1 was used during mechanical milling. The high energy milling was performed in two stages as shown in the schematic diagram (Fig. 1). In the first stage of milling, the impeller was set to rotate at 1300 rpm for the first 45 s and followed by 700 rpm for the next 15 s in every minute. This could be an effective way to achieve a high degree of homogeneous nanoscale composite powders with little or no contamination. It is expected that the cyclic milling process in the first stage of milling can effectively fragment the Si-$FeSi_2$ powders due to repetitive impact of the milling media and powder resulting from high and low kinetic energy supply. In the case of conventional low-speed milling, serious contamination is commonly observed with lengthening in milling time. The cyclic milling process was continued for 10 h during the first stage milling to achieve the nano-scale Si embedded $FeSi_2$ phase (Si-$FeSi_2$). For a second stage milling, 15 at% carbon powder was mixed with the milled Si-$FeSi_2$ powders and then the mixed powders were further milled for 6 h at constant rotation speed 500 rpm to besiege Si-$FeSi_2$ nanocomposite powders with carbon layer (termed as Si-$FeSi_2$/C) as depicted in the schematic diagram.

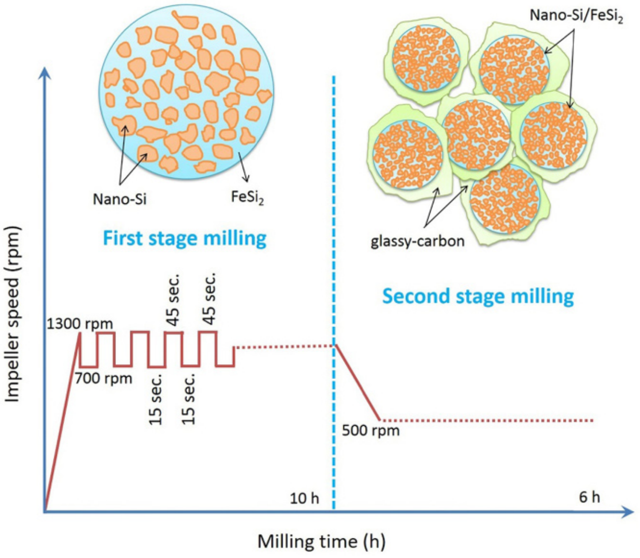

Fig. 1. Schematic illustration of the experimental process of fabricating Si-$FeSi_2$/C nanocomposite powders by two-stage high-energy mechanical milling.

2.2. Material characterization

The crystalline structures were studied using an X-ray diffractometer (Mini Flex 600; Rigaku) with Cu-Kα radiation ($\lambda = 1.5418$ Å) operating at 600 W with a step size of 0.02° from 10 to 90° in the 2θ range. The specific surface area was determined from N_2 adsorption isotherms using the multipoint Brunauer-Emmett-Teller (BET) method (BET, ASAP 2020, ProTech Korea). Field-emission scanning electron microscopy (FE-SEM; MIRAH, TESCAN) and transmission electron microscopy (TEM; Tecnai G2 F30, FEI) were used to observe the morphology of the milled powders and the coin cells produced from them. Raman analysis was carried out at room temperature with the LabRAM HR UV/Vis/NIR Raman spectrometer (HORIBA Jobin Yvon, France). Raman spectra were recorded over a Raman shift range of 300 to 2000 cm^{-1}; He-Ar laser (514.5 nm) was employed as the excitation source and the laser power was set to 200 mW.

2.3. Electrochemical measurements

For the electrochemical evaluation, the milled nanocomposite electrodes were prepared in the form of coin-cells (half-cells) by coating Cu substrates with a slurry containing the following materials dissolved in N-methyl-2-pyrrolidinone (NMP): the active material (80 wt%), SFG6 graphite (10 wt%), Ketjenblack conductive agent (2 wt%), and polyamide-imide binder material (PAI, 8 wt%). The electrodes were printed on Cu foil and dried at 110 °C for 10 min. After drying, they were cut into 16-mm-diameter discs and subsequently, heat treated at 350 °C for 2 h under vacuum. Coin-type electrochemical cells were assembled in an Ar-filled glove box. Celgard® 2400 was used as the separator; lithium foil was used as both the counter and reference electrodes. The electrolyte was a 1 M solution of lithium hexafluorophosphate ($LiPF_6$) dissolved in a mixture of ethylene carbonate (EC)/diethyl carbonate (DEC)/ fluoroethylene carbonate (FEC) (5:70:25 by volume). The cells were charged and discharged using a battery charge/discharge test system (WBCS3000L, WonATech Co., Ltd.) in the cut-off potential ranges of 0.01-2.0 V (under constant current density of 2.5 mA cm^{-2}) at 0.1 and 0.2 C-rate for the first and second cycles respectively, and 1.0 C-rate from the third cycle.

3. RESULTS AND DISCUSSION

3.1. Nanocomposite structure evolution

Figure 2 shows the X-ray diffraction (XRD) profiles of the Si-$FeSi_2$ and Si-$FeSi_2$/C nanocomposite powders. The X-ray diffraction peaks of the pre-alloyed powders (Fig. 2(a)) consists of Si (2Θ = 28.5°, 47.4°, and 56.0°) and $FeSi_2$ (2Θ = 17.2°, 37.9°, and 49.1°), indicating two-phase formation of Si and $FeSi_2$. It is evident that the sharp peaks of the Si and $FeSi_2$ phases became weak and broad after milling the pre-alloyed powder for 6 and 10 h, during the first stage of milling. In particular, the Si-peak intensities were significantly reduced compared to the $FeSi_2$ peaks, implying the refinement and formation of Si nanocrystals. In the second stage milling, the Si-$FeSi_2$ powders further milled for 6 h with the carbon (graphite), a weak diffraction peak has been observed at 2Θ = 26.4 (Fig. 2(b)). The corresponding graphite peak intensity was abruptly decreased with milling time when compared to the initial graphite peak. It has been reported that the crystallite size of pure graphite can be greatly reduce to about 1.5 nm due to a crumbling effect during high-energy mechanical milling [29]. However, since the Si-peak intensity was not changed by the further milling, the Si crystal size was expected to be unchanged. Besides, any diffraction peaks related with the contamination such as Fe or different silicide phases were not observed from the X-ray diffraction results.

The micrographs of the pre-alloyed and nanocomposite powders are shown in Fig. 3. The pre-alloyed powders comprised of irregular shapes and non-uniform size distribution with a maximum particle size of about 100 μm. After 10 h milling, the powder size was significantly reduced through the repetitive milling process of cold welding and fragmentation (Fig. 3(b)). The Si-$FeSi_2$/C composite powder micrograph (Fig. 3(c)) revealed relatively a smooth surface comparing to the rough surface of Si-$FeSi_2$ powder, which can be plausibly due to the surface friction between Si-$FeSi_2$ and graphite carbon. From the XRD results (which showed a dramatic reduction in graphite peak intensity without any noticeable changes in Si and $FeSi_2$ peaks) and SEM micrographs of Si-$FeSi_2$/C, it is believed that the further mechanical milling for 6 h leads to

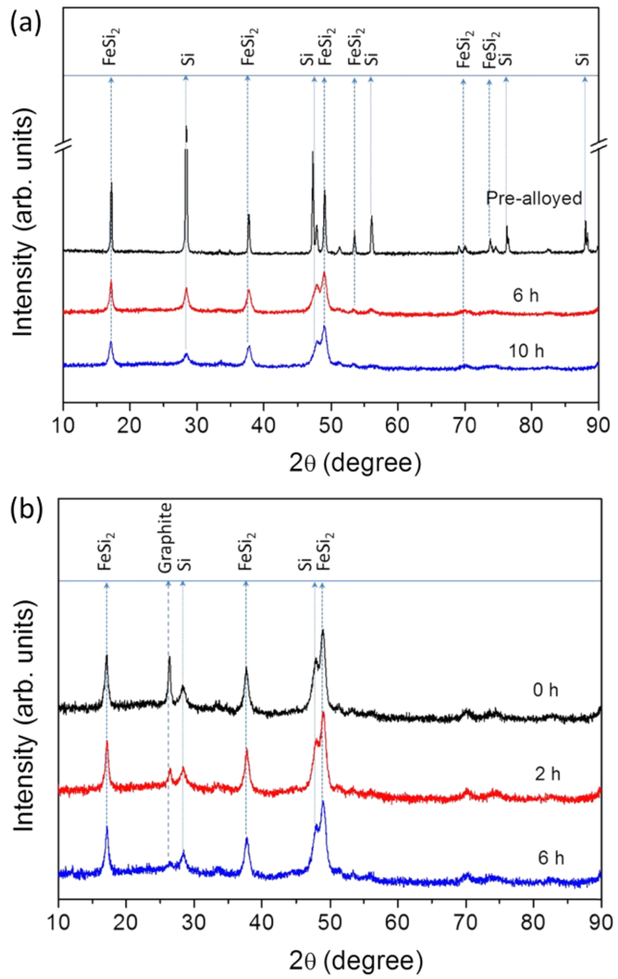

Fig. 2. Evolution of X-ray diffraction patterns of (a) Si-$FeSi_2$ and (b) Si-$FeSi_2$/C powders at different milling times.

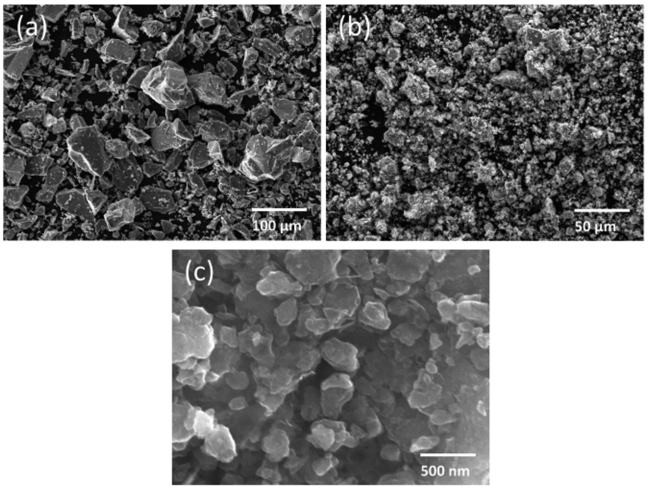

Fig. 3. Field-emission scanning electron microscopy images showing the powder morphology of: (a) pre-alloyed powders; (b) Si-$FeSi_2$ powders milled for 10 h; (c) Si-$FeSi_2$/C powders milled for 6 h.

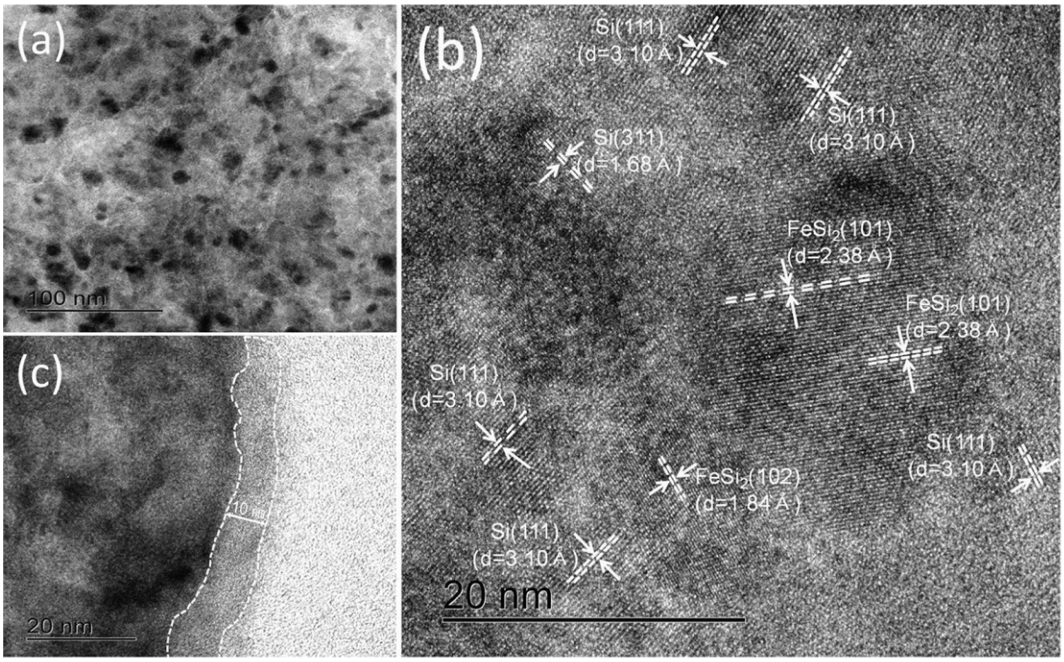

Fig. 4. Transmission electron microscopy images of Si-FeSi$_2$/C powders milled for 6 h: (a) internal microstructure; (b) high-resolution TEM image; (c) magnification of the Si-FeSi$_2$ and carbon interface microstructure.

the formation of carbon layer over the Si-FeSi$_2$ powder. In addition, such a secondary milling (with carbon powders) was effective to achieve the random distribution and dispersion of Si-FeSi$_2$/C composite powders. The specific surface area of the powders determined through BET method is 4.47 and 13.71 m^2 g^{-1} for Si-FeSi$_2$ and Si-FeSi$_2$/C respectively. According to the results, the specific surface area of the Si-FeSi$_2$/C is three times larger than Si-FeSi$_2$, which indicating that the Si-FeSi$_2$/C exhibit smaller particle size due to the increasing milling time through second stage milling.

Figure 4 shows the TEM images with the high-resolution lattice pattern of the Si-FeSi$_2$/C nanocomposite. Figure 4(a) shows an overlapped microstructure, which is typical in nanocomposite powder produced by high-energy mechanical milling processes. The active nano-Si (white region) was randomly distributed between FeSi$_2$ matrix phases (gray-black regions). From the high-resolution TEM image (Fig. 4(b)), it is obvious that the nanocomposite mainly comprised of nano-crystalline Si and FeSi$_2$ phases along with partially amorphous phase; Si nano-crystals seemed to lose their crystallinity with longer milling time and hence the amorphous Si phase is expected. The inter-planar distance (d) of the nanocrystals was estimated as shown in Fig. 4(b) and the corresponding phases were identified as Si and FeSi$_2$ by comparing the measured d values with the theoretical values provided by the Joint committee for Powder Diffraction Standards (JCPDS) data. No trace of carbon was observed in the internal microstructure of the nanocomposite powder, which indicated no impregnation of carbon into the matrix phase during the secondary milling. Based on the interfacial microstructure Fig. 4(c) between Si-FeSi$_2$ and the carbon layer (about 10 nm thick), it is evident that carbon built a surface layer on the Si-FeSi$_2$ powder rather than impregnating into Si-FeSi$_2$ matrix. However, the carbon layer was not distinctly crystalline. The chemical structure of the carbon layer was investigated by Raman spectroscopy (Fig. 5). The sharp peak at 520 cm^{-1} was attributed to the crystalline silicon, and the two peaks obtained at 1350 and 1580 cm^{-1} are assigned to the amorphous carbon and the crystalline graphite materials respectively [30,31]. It is known that the Raman spectra of carbon materials are typically characterized by a pair of bands called G-band (graphitic) and D-

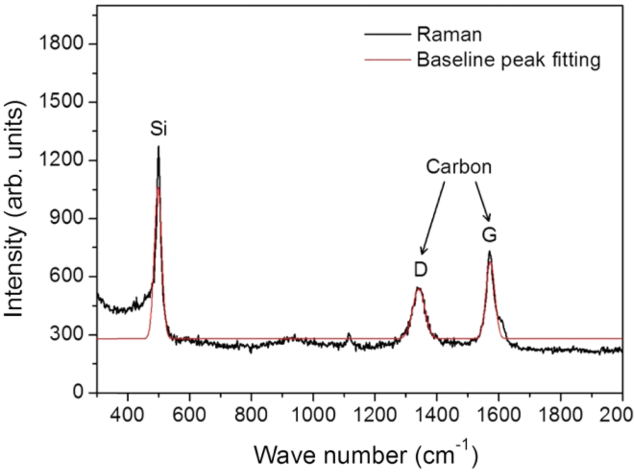

Fig. 5. Raman spectra of Si-FeSi$_2$/C nanocomposite powder milled for 6 h.

band (disordered). The peak appeared at 1580 cm^{-1} (G band) was a result of the in-plane carbon to carbon stretching vibration mode, E_{2g}, of the well-crystallized graphite. Whereas, the broad peak at 1350 cm^{-1} (D band) was assigned to the disordered *sp2* phase mode, A_{1g}, of the edge plane [32-34]. The Raman intensity ratio, R, intensity of the D-band (I_D) to that of G-band (I_G) varies depending on the structure of the carbon and it designates the degree of disordering of the crystal structure of the carbon surface. The ratio R calculated by the Gaussian function fitting was found to be 0.74, which indicating the presence of lower volume fraction of the defect or amorphous carbon. This suggests the crystalline graphitic carbon is more prevalent than the defect-oriented carbon phase. Hence, a good electrical contact can be anticipated between the active materials.

3.2. Electrochemical performance

The electrochemical characteristics of Si-$FeSi_2$ and Si-$FeSi_2$/C nano-composites were evaluated using coin-type half-cells. Voltage profiles of the 1st, 2nd, 4th, and 20th cycle are shown in Fig. 6(a) and 6(b). Flat plateaus were observed in the lithiation curves of both electrodes at ~0.25 V. This corresponds to the lithiation process of crystalline Si to form the amorphous Li_xSi phase and the formation of the solid electrolyte interface (SEI) [35]. The delithiation curves of the Si-$FeSi_2$ were significantly shifted towards lower capacity side with respect to cycle number, and exhibited an irreversible capacity loss of about 13.53%, 3.2%, and 1.4% during the 1st, 2nd, and 4th cycles respectively. Such a discharge curve shift after the first cycle can be attributed to the phase transformation of the active silicon from crystalline to amorphous during lithiation and SEI formation [36,37]. However, discharge curves of the Si-$FeSi_2$/C were perceived to be shifted very less as compared to that of Si-$FeSi_2$ electrode. In addition, overlapping of the discharge curves during 1st and 2nd cycles can be seen from Fig. 6(b), indicates stable lithiation and delithiation which can be anticipated due to the reason of stable SEI formation over the carbon but not only on active Si. Thus, the lithium-ion can find easy path for alloying and de-alloying with silicon. The irreversible capacity loss of Si-$FeSi_2$/C during 1st, 2nd, and 4th cycles is 19.32%, 4.7%, and 1.1% respectively. Although irreversible capacity loss during the initial and second cycles is higher, the Si-$FeSi_2$/C exhibited lower irreversible capacity loss than Si-$FeSi_2$ (~0.5%) in the subsequent cycles. In addition, the formation of an SEI layer is accompanied by the consumption of a certain amount of lithium; therefore, the coulombic efficiency reached ~99.5% within the first 5 cycles.

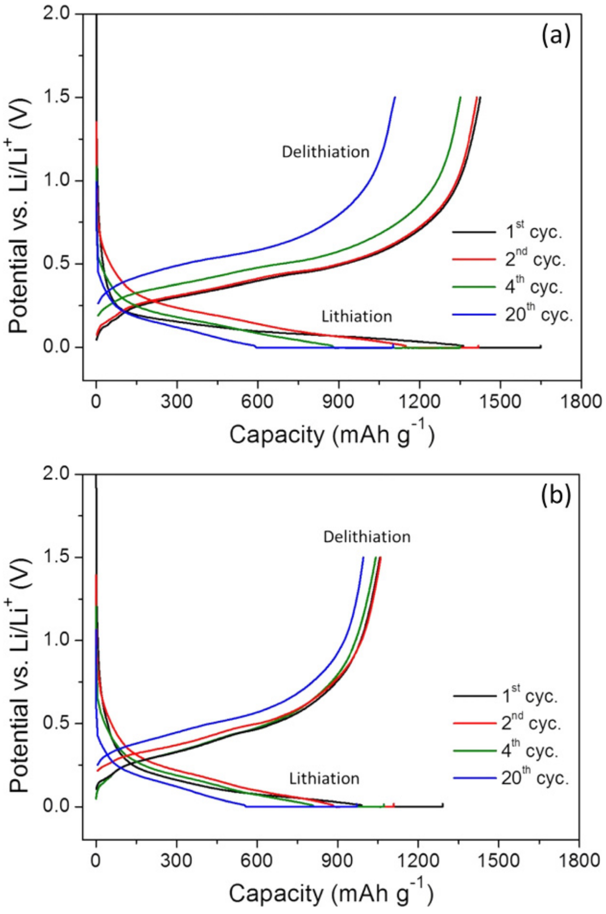

Fig. 6. Voltage charge-discharge profiles of nanocomposite electrodes at different cycle number: (a) Si-$FeSi_2$; (b) Si-$FeSi_2$/C.

Figure 7 shows the capacity and coulombic efficiency with respect to cycle number. The initial cycle (0.1 C-rate) capacities of Si-$FeSi_2$ and Si-$FeSi_2$/C electrodes are 1659.3 and 1321.6 mAh g^{-1}; and the corresponding coulombic efficiency (C/D efficiency) of the electrodes are 86.47% and 80.68%, respectively. The low initial cycle capacity and coulombic efficiency of Si-$FeSi_2$/C are attributed to the reduced Si content and Li-ion loss caused by SEI formation on the larger specific surface area (13.71 m² g^{-1}). Moreover, a larger amount of lithium ions will be irreversibly transported and isolated through the

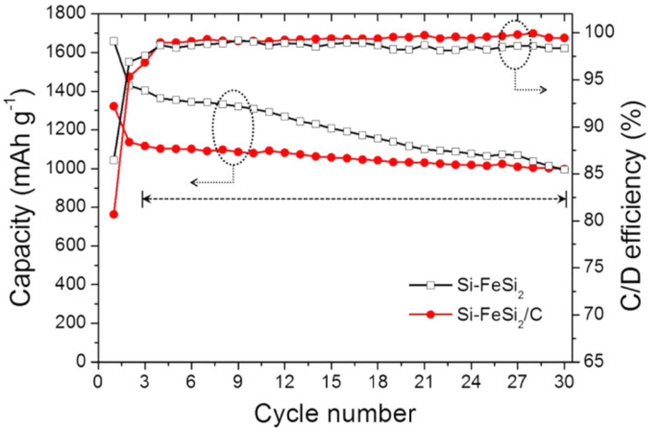

Fig. 7. Electrochemical performance: Capacity and coulombic efficiency versus cycle number of Si-$FeSi_2$ and Si-$FeSi_2$/C nanocomposite electrodes.

graphite carbon [38]. The cyclic profile shows that the coin-cell with Si-FeSi$_2$ nanocomposite powder shows severe capacity fading with increasing cycle number, which is due to the large amount of active Si content, Si size, poor electrical conductive path, and unstable SEI formation [36,37]. Also, theoretically the active Si phase fraction was expected to be about 55% based on lever rule. The Si was surrounded by the less active and electrically poor conductive FeSi$_2$ phase. The SEI on Si is relatively thick and unstable, since during delithiation, the Si particle shrinks, and the SEI layer breaks down into separate pieces, and fresh Si surface is exposed to the electrolyte. In later cycles, new SEI layer continues to be formed on the newly exposed silicon surfaces. The thick SEI layer is harmful for the cycle life, because it can cause a rise of the electrode impedance/polarization and decrease of the electrode's electrochemical reactivity [39]. The Si-FeSi$_2$/C electrode exhibits excellent capacity retention and lower capacity fading along with prominent coulombic efficiency ~99.5%. In fact, the active Si crystal size was ~20 nm (from Fig. 4(c)) which can be beneficial to decrease volume changes, shorten the Li-ion diffusion path and available large surface area [40,41]. In addition, the added carbon could provide a conductive channel in the form of graphite carbon phase for electron transport, act as a buffer to alleviate the volume changes during cycling, which can be achieved by the interphase sliding between active Si and graphene layer in graphite carbon phase [42]. Besides, the SEI was expected to be thin and mechanically stable due to the reduced volume changes without critical failure during the cycling. As described in the analysis of Raman spectra, the Raman ratio *R* of 0.74 evidently confirmed that all the aforementioned benefits of graphene were coordinated to improve the electrochemical performance of the Si-FeSi$_2$/C electrode. Based on these observations it is concluded that the Li-ions can easily diffuse in/out to the graphite phase while alloying/dealloying (lithiation/delithiation) with Si during the cycling. Therefore, good capacity retention was achieved by the nanocomposite structured Si-FeSi$_2$/C.

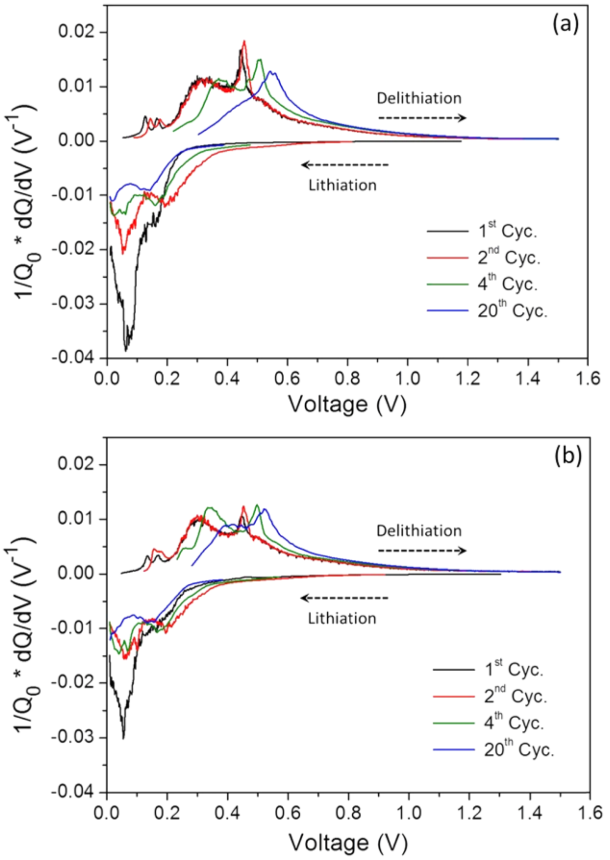

Fig. 8. Differential capacity plots of nanocomposite electrode at different cycle number: (a) Si-FeSi$_2$; (b) Si-FeSi$_2$/C.

The differential capacity plots (DCPs) during the 1st, 2nd, 4th and 20th cycle of both Si-FeSi$_2$ and Si-FeSi$_2$/C nanocomposite electrodes are shown in Fig. 8(a) and 8(b), respectively. The sharp peak obtained at ~0.062 and ~0.054 V in both Si-FeSi$_2$ and Si-FeSi$_2$/C corresponds to the formation of alloyed Li-Si phase of Li$_{15}$Si$_4$, which is in agreement with the previous reports on pure Si [43,44]. And the peaks appeared during the first and second cycles at 0.3, 0.38, and 0.45 correspond to the de-alloying of lithium [25]. In addition, the two broad peaks that appeared during delithiation (~0.5 and 0.55 V) indicate the conversion of crystalline silicon to an amorphous state after the first cycle [45,46]. The peaks appearing near 0.12 and 0.2 V during the delithiation/lithiation cycles represent the intercalation and de-intercalation of Li-ion into graphite [47]. As shown in Fig. 8(b), during the first cycle, the intensity of the Si lithiation peak of Si-FeSi$_2$/C was significantly decreased at ~0.056 V suggest that the less amount of lithium-ion alloying with Si as compared to that of Si-FeSi$_2$; also, the peak broaden at ~0.2 V is due to Li-alloying with graphite. In addition, during the delithiation, two broad peaks were observed, resulting from the overlapping of at least two possible reaction processes (Li$_{22}$Si$_5$ and Li$_{15}$Si$_4$) based on the two peaks appearing in the delithiation process; similar observations were reported [48]. It is believed that the peak intensity corresponds to the reaction of lithium with silicon [49]. The intensities of the Si delithiation peaks in Si-FeSi$_2$ were gradually decreased with respect to the cycle number, indicating retarded Li-ion reaction with active silicon, which can be not only due to the amorphization of active Si but also Si isolation by the surrounding less-active FeSi$_2$ phase or thicker SEI formation. However, in Si-FeSi$_2$/C, the intensities of Si peaks during the delithiation after first cycle were observed to be almost similar, which is evident for the constant lithiation/delithiation due to both good contact between the active materials and stable SEI formation, which effectively contributes for high capacity retention of the electrode [50].

The coin-cell internal and crystal structure of the Si-FeSi$_2$/C electrode after the 1st and 30th cycle were studied using TEM, as shown in Fig. 9. The internal microstructure (Fig. 9(a))

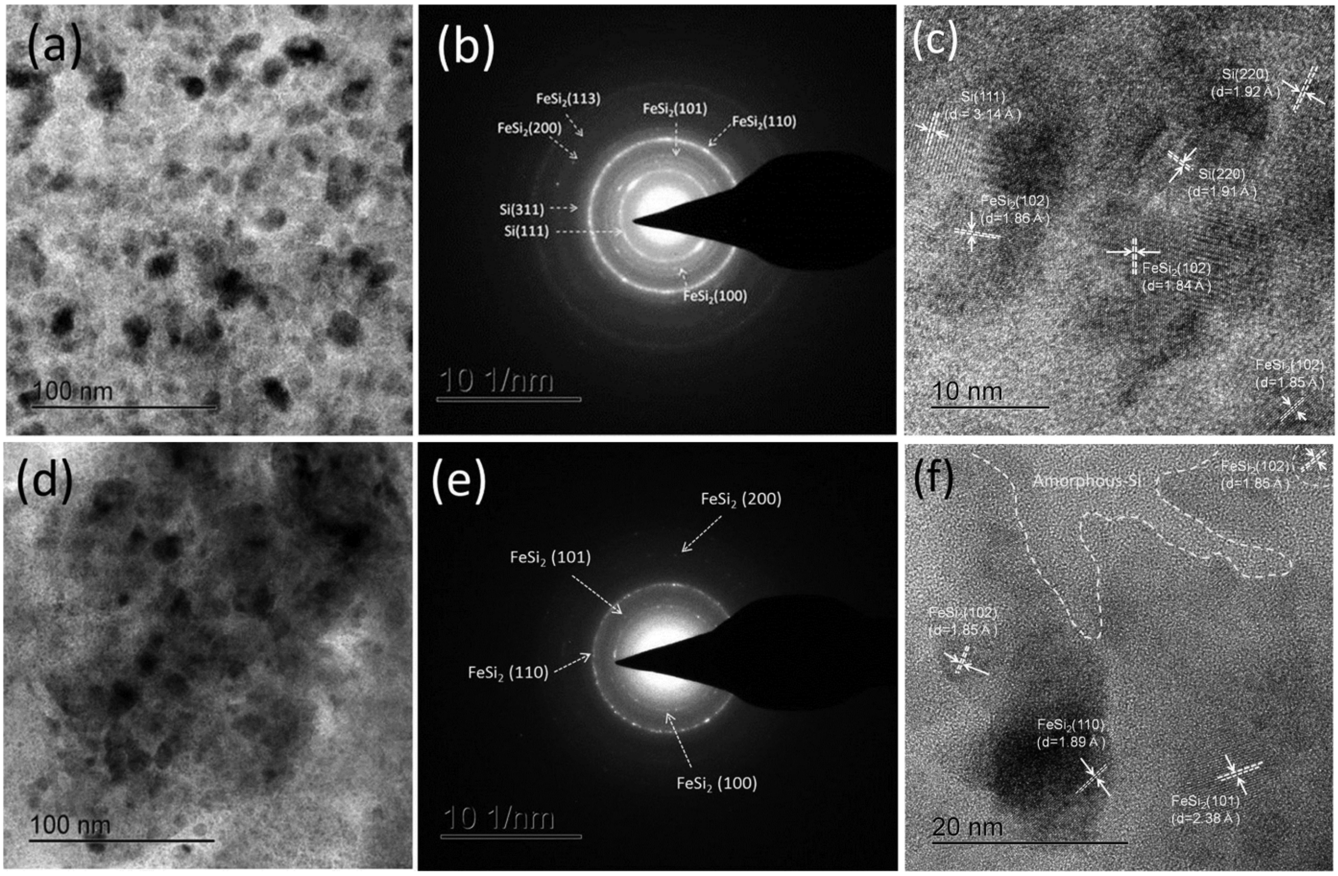

Fig. 9. Structural evolution of the Si-FeSi$_2$/C nanocomposite electrodes after and before cycling: after 1st cycle (a, b, and c); after 30th cycle (d, e, and f).

after the first cycle shows a well distributed nanocomposite with Si and FeSi$_2$ phase. The corresponding selected area electron diffraction (SAED) ring patterns indicate the presence of Si and FeSi$_2$ phases (Fig. 9(b)). In addition, the existence of nanocrystalline Si and FeSi$_2$ phases are definite from the high-resolution lattice image Fig. 9(c), respective interplanar distance (*d*) was calculated and confirmed with the standard JCPDS data. However, the disintegration of nano-Si during the charging/discharging was observed after the 30th cycle (Fig. 9(d)), which was believed to be due to the phase change of Si from nanocrystalline to amorphous phase. The relevant SAED ring pattern (Fig. 8(e)) shows that the Si pattern was completely diffused and faded out, which indicating the amorphous phase. However, the FeSi$_2$ phase maintained its crystallinity even after the 30th cycle. The high-resolution image shows a few FeSi$_2$ nanocrystals embedded in amorphous Si matrix, in which active Si is coalesced with neighboring amorphous network. Since larger Si phase is unfavorable to accommodate the volume changes, and the restrained growth of amorphous Si will be desirable for capacity retention. Accordingly, further studies are required for clear understandings on the effect of extended network type amorphous Si phase growth on electrochemical behavior.

4. CONCLUSION

We have synthesized Si-FeSi$_2$/C nanocomposite powders through a two-stage milling process. The first-stage high-energy mechanical milling was effective to fragment Si and FeSi$_2$ phase and then the milled Si-FeSi$_2$ powders were covered with carbon layer driven by the secondary milling, in which no detectable contamination was observed. The role of the carbon layer was to form a stable Solid Electrolyte Interface (SEI) and electronic conduction path. The Si-FeSi$_2$/C delivers a discharge capacity of 1082 mAh g^{-1} with a significant coulombic efficiency of 99.5%. The Raman ratio *R* value of 0.74 observed from the Si-FeSi$_2$/C nanocomposite powders indicates a higher fraction of graphite phase, which can be beneficial to improve the electrochemical performance by providing a strong conducting path along with its high mechanical flexibility. Consequently, enhanced capacity retention of the Si-FeSi$_2$/C nanocomposite wherein nano-sized active Si is well-dispersed in the carbon supported FeSi$_2$ matrix phase was presumed to be due to the refinement of the Si crystal, the stable SEI and electrical conducting pathway provided by graphite phase, which was achieved by two-stage mechanical milling.

ACKNOWLEDGEMENT

This research was partially supported by graphite exfoliation system in the Functional Districts of the Science, Belt support program, Ministry of Science ICT and Future Planning (2015K000281).

REFERENCES

1. P. G. Bruce, B. Scrosati, and J. M. Tarascon, *Angew. Chem. Int. Edit.* **47**, 2930 (2008).
2. M. Armand and J. M. Tarascon, *Nature* **451**, 652 (2008).
3. E. Yoo, J. Kim, E. Hosono, H. Zhou, T. Kudo, and I. Honma, *Nano Lett.* **8**, 2277 (2008).
4. J. M. Tarascon and M. Armand, *Nature* **414**, 359 (2001).
5. B. Kang and G. Ceder, *Nature* **458**, 190 (2009).
6. N. S. Choi, Z. Chen, S. A. Freunberger, X. Ji, J. Cho, G. B. Peter, *et al. Angew. Chem. Int. Edit.* **51**, 9994 (2012).
7. M. Winter, J. O. Besenhard, M. E. Spahr, and P. Novak, *Adv. Mater.* **10**, 725 (1998).
8. S. Y. Hong, Y. Kim, Y. Park, A. Choi, N. Choic, and K. T. Lee, *Energ. Environ. Sci.* **6**, 2067 (2013).
9. H. Jung, M. Park, Y. G. Yoon, G. B. Kim, and S. K. joo, *J. Power Sources* **115**, 346 (2003).
10. J. R. Szczech and S. Jin, *Energ. Environ. Sci.* **4**, 56 (2011).
11. H. Wu and Y. Cui, *Nano Today* **7**, 414 (2012).
12. M. T. McDowell, S. W. Lee, W. D. Nix, and Y. Cui, *Adv. Mater.* **25**, 4966 (2013).
13. F. Cheng, J. Liang, Z. Tao, and J. Chen, *Adv. Mater.* **23**, 1695 (2011).
14. L. F. Cui, R. Ruffo, C. K. Chan, H. L. Peng, and Y. Cui, *Nano Lett.* **9**, 491 (2009).
15. Y. L. Zhou, X. L. Jiang, L. Chen, J. Yue, H. Y. Xu, J. Yang, *et al. Electrochim. Acta* **127**, 252 (2014).
16. Y. Yao, M. T. McDowell, I. Ryu, H. Wu, N. Liu, Y. Cui, *et al. Nano Lett.* **11**, 2949 (2011).
17. M. K. Datta, J. Maranchi, S. J. Chung, R. Epur, K. Kadakia, P. N. Kumta, *et al. Electrochim. Acta* **56**, 4717 (2011).
18. S. B. Son, S. C. Kim, C. S. Kang, T. A. Yersak, Y. C. Kim, S. H. Lee, *et al. Adv. Energy Mater.* **2**, 1226 (2012).
19. H. W. Yang, J. H. Lee, S. C. Jung, S. T. Myung, W. S. Kang, and S. J. Kim, *Korean J. Met. Mater.* **54**, 780 (2016).
20. C. Loka, H. Yu, K. S. Lee, and J. S. Cho, *J. Power Sources* **244**, 259 (2013).
21. Y. Yu, L. Gu, C. Zhu, S. Tsukimoto, P. A. Aken, and J. Maier, *Adv. Mater.* **22**, 2247 (2010).
22. B. D. Polat, O. Keles, and K. Amine, *Nano Lett.* **15**, 6702 (2015).
23. T. Kasukabe, H. Nishihara, S. Iwamura, and T. Kyotani, *J. Power Sources* **319**, 99 (2016).
24. Y. Chen, J. Qian, Y. Cao, H. Yang, and X. Ai, *ACS Appl. Mater. Interfaces* **4**, 3753 (2012).
25. H. T. Yu, C. Loka, K. S. Lee, J. S. Cho, and S. H. Lee, *Mater. Sci. Eng. B* **178**, 1422 (2013).
26. H. R. Park, Y. J. Kwak, S. H. Lee, and M. Y. Song, *Korean J. Met. Mater.* **54**, 916 (2016).
27. S. Jung, H. Kwon, K. M. Roh, C. Y. Suh, and W. Kim, *Met. Mater. Int.* **21**, 923 (2015).
28. C. Suryanarayana, *Prog. Mater. Sci.* **46**, 1 (2001).
29. C. S. Wang, G. T. Wu, X. B. Zhang, Z. F. Qi, and W. Z. Li, *J. Electrochem. Soc.* **145**, 2751 (1998).
30. Y. Kawashima, *Phys. Rev. B* **52**, 10053 (1995).
31. M. Yoshikawa, G. Katagiri, H. Ishida, and A. Ishitani, *Solid State Commun.* **66**, 1177 (1988).
32. R. J. Nemanich and S. A. Solin, *Phys. Rev. B* **20**, 392 (1979).
33. H. Groult, T. Nakajima, N. J. Kumagai, L. Perrigaud, Y. Ohzawa, H. Yashiro, *et al. J. Fluorine Chem.* **126**, 1111 (2005).
34. J. Nanda, M. K. Datta, J. T. Remillard, A. O'Neill, and P. N. Kumta, *Electrochem. Commun.* **11**, 235 (2009).
35. M. T. McDowell, I. Ryu, S. W. Lee, C. Wang, W. D. Nix, and Y. Cui, *Adv. Mater.* **24**, 6034 (2012).
36. M. N. Obrovac and L. Christensen, *Electrochem. Solid St.* **7**, A93 (2004).
37. L. Y. Beaulieu, T. D. Hachard, A. Bonakdarpour, M. D. Fleischauer, and J. R. Dahn, *J. Electrochem. Soc.* **150,** A1457 (2003).
38. S. H. Ng, J. Wang, D. Wexler, K. Konstantinov, Z. P. Guo, and H. K. Liu, *Angew. Chem. Int. Edit.* **45**, 6896 (2006).
39. D. Ma, Z. Cao, and A. Hu, *Nano-Micro Lett.* **6**, 347 (2014).
40. P. G. Bruce, B. Scrosati, and J. M. Tarascon, *Angew. Chem. Int. Edit.* **47**, 2930 (2008).
41. J. R. Szczech and S. Jin, *Energ. Environ. Sci.* **4**, 56 (2011).
42. I. H. Son, J. H. Park, S. Kwon, S. Park, M. H. Rummeli, H. Chang, *et al. Nat. Commu.* **6**, 7393 (2015).
43. P. Limthongkul, Y. Jang, N. J. Dudney, and Y. M. Chiang, *Acta Mater.* **51**, 1103 (2003).
44. J. Li and J. R. Dahn, *J. Electrochem. Soc.* **154**, 1765 (2007).
45. H. K. Han, C. Loka, Y. M. Yang, J. H. Kim, S. W. Moon, K. S. Lee, *et al. J. Power Sources* **281**, 293 (2015).
46. I. Kim, G. E. Blomgren, and P. N. Kumta, *J. Power Sources* **130**, 275 (2004).
47. M. Su, Z. Wang, H. Guo, X. Li, S. Huang, L. Gan, *et al. Powder Technol.* **249**, 105 (2013).
48. S. Yoo, J. Lee, S. Ko, and S. Park, *Nano Energy* **2**, 1271 (2013).
49. Q. Peng, C. Yungui, Z. Ding, X. Chenghao, H. Lihong, and D. Xiaobo, *Rare Metal Mater. Eng.* **43**, 1073 (2014).
50. S. Chou, J. Wang, M. Choucair, H. Liu, J. Stride, and S. Dou, *Electrochem. Commun.* **1**, 1079 (2010).